# Numerical simulation at the micro-scale for the heat transfer modelling in the thermoplastic composites laser-assisted AFP process

Adrien Le Reun, Violaine Le Louët, Steven Le Corre, Vincent Sobotka

# Numerical simulation at the micro-scale for the heat transfer modeling in the thermoplastic composites laser-assisted AFP process

Adrien Le Reun, Violaine Le Louët, Steven Le Corre, Vincent Sobotka

*Nantes Université, CNRS, Laboratoire de Thermique et énergie de Nantes, LTeN, UMR6607, F-44000, Nantes, France*

**Abstract**

Laser-assisted Automated Fibre Placement for thermoplastic composites has shown its potential to process complex shaped parts with high productivity rates but many challenges, both physical and technical, still need to be adressed in order to achieve proper in-situ consolidation. Ensuring high quality bonding of the laid tapes relies on perfect control of their thermal history throughout the process, and heat transfer has long proven essential to achieve this. Numerous heat transfer models account for optical interaction between the laser and composite at a macroscopic scale. Here, a thermo-optical model at the micro-scale is designed and differentiates the fibres from matrix domain, accounting for their respective properties. A single tape is modeled in a static configuration. Based on a composite material realistic microstructure, a ray-tracing algorithm highlights the laser heat absorption depth dependency to laser incidence angle and fibre distribution. Numerical surface temperatures are compared to experimental data obtained with a specific set-up leading to an overall accurate approximation. Finally, the microstructure model relevance is assessed with 1D homogenised models considering either ideal surface heating or a volumetric heat source. The surface heating model leads to inaccurate approximation of surface temperatures, whereas volumetric heat source absorption substantially limits temperature errors. As a result, this model gives a satisfactory compromise between model complexity, computational time and temperature prediction.

*Keywords:*

A. Polymer-matrix composites (PMCs)

B. Optical properties/techniques

C. Finite element analysis (FEA)

E. Automated fibre placement (AFP)

## 1. Introduction

Pushed by aeronautical needs, the interest for thermoplastic composite materials (TPC) has increased a lot over the past decade. Among the different reasons for their current success, their ability to melt and undergo several forming steps, as well as their healing capability, makes them more attractive than usual thermoset polymer composites for aeronautical applications. In the large family of TPC forming techniques, the Automated Fibre Placement (AFP) process has been pointed out as a suitable solution to meet the expectations of complex shapes and high performance materials for aeronautical parts. The process, based on the laying of narrow prepreg tapes with automated systems, is promising to enable the manufacturing of complex shapes with an in-situ consolidation. The simplification of the process in three steps is depicted in Fig. 1: heating, adhesion and cooling. First, the laying tape and substrate are heated to reach the matrix melting temperature and then pressurized by a compaction roller in order to increase their intimate contact. Bonding of ply and substrate occurs with the inter-diffusion of polymer chains through the interface, called reptation [1]. Finally, consolidation continues in the cooling phase, during which thermoplastic crystallization occurs. In this technique, laser/composite interaction is the key parameter in order to control both the heating and the adhesion process, and eventually move towards in-situ consolidation, that would enable acceptable material health, getting rid of the costly and time-consuming post-consolidation step. Heating systems [2, 3] have been developed to fit the process constraints. Laser diode has been identified as the most suitable heating system supplying a focused powerful beam with a short response time and the ability to be easily controlled. The objective of the laser-assisted AFP process is to compete with autoclave consolidation in terms of manufacturing quality. To reach this goal, the understanding and modeling of heat transfer and material thermal history are fundamental to ensure that the ply and substrate reach the matrix melting temperature without exceeding the matrix degradation temperature [4–6]. The quality of the adhesion phase also relies on the temperature field to maximize the degree of intimate contact and limit inter-layer thermal contact resistances [7–12]. Therefore, a precise heat transfer model is required to predict ply and substrate temperatures and thermal history.

Many studies [13–19] consider heat exchange in the process configuration in which substrate and ply are modeled. Two kinds of models have been studied with different approaches. In the first case, from a process point-of-view, an area prior to the nip-point is studied corresponding to a continuous laying configuration. A steady state is considered for constant laying speed and geometries [13, 15]. In the second case, the model focuses on the temperature evolution of an area of the laying tape [15, 17]

through the whole laying process from the heating phase to consolidation.

Grove [20] was the very first to try to model heat transfer during the AFP process considering an anisotropic but homogeneous material in a Finite Element Method (FEM) simulation. More recently, laser interaction with the composite has been deeply investigated using ray-tracing algorithms to measure the distribution of heat flux in ply and substrate [15–19, 21]. Grouve [15] includes heat exchanges with the compaction roller and tooling with a more complex optical model which computes reflections on the substrate and the laying tape. Stokes-Griffin et al. [21] characterized the optical behavior of a carbon fibre reinforced thermoplastic composite for a near-infrared laser heating process. The scattering behavior of the composite with angular dependent reflectance has been highlighted and compared with a micro-cylinder absorption model at the scale of the fibre. Based on these properties, a combined optical and thermal model has been developed [17] considering reflections and the shadow area occurring prior to the nip-point. Dolo et al. [16] computed composite reflectance using Snell-Descartes laws. An absorption depth of 0.3 $\mu m$ was then calculated using Beer-Lambert law for the laser wavelength. A ray-tracing model is used to compute the first incidence and the two following reflections between ply and substrate. Baho et al. [18] took into account the roller deformation to improve the absorption model with reflections and found that roller deformation modifies the heat flux and consequently temperature distribution on substrate. Results show that ray reflections, especially the first one, have a substantial effect on substrate and laying tape temperatures. Baho et al. [19] used a similar thermo-optical model for a hybrid material and integrated inter-layer thermal contact resistances based on a degree of intimate contact model [9]. Experiments with inter-layer thermocouples and an infrared camera were conducted to assess the quality of the model. Cosson et al. [22] initiated microscale model of laser absorption by studying the effect of microstructure variability on the homogenised thermal properties of a glass fibre-reinforced thermoplastic. They used a ray-tracing algorithm to measure local scattering absorption. The influence of process parameters on thermal history of substrate and tape is simulated with the thermal models.

To sum up, the state of the art points out the variety of numerical studies to model heat transfer in the AFP process. Most studies are based on a homogeneous model considering anisotropic properties and assuming that the heterogeneity of the microstructure is negligible and can be simplified with an equivalent homogeneous material. No description of temperature field or heat transfer is provided at the scale of the microstructure. Thermal properties such as thermal conductivity or specific heat capacity are either directly measured on prepreg or determined using equivalent homogeneous models.

Anisotropic behavior of the composite which is caused by carbon fibre anisotropy exhibiting a higher thermal conductivity in fibre direction (around 10 times higher) than in transverse direction [23] are taken into account using analytical or numerical models [24–27].

Most of the studies model laser heating by a surface flux condition, considering that laser flux is supposedly absorbed in surface. However, heating and cooling kinetics are not perfectly described leading to an inaccurate estimation of surface temperatures. Moreover, a simplification of material properties through homogenisation is performed. As a result, the effects of microstructure on heat transfer such as the differences in fibre and matrix thermal properties are not taken into account. Upgrading from mesoscale to microscale to overcome these issues is an interesting path to investigate.

The novelty of this article is the design of a thermo-optical model at the micro-scale. A single tape heated by laser in a static configuration is considered. The choice of a very simple configuration has been made to focus on heat transfer kinetics in the laser heating of a prepreg tape with a reliable experimental assessment conducted thanks to a specific designed apparatus. The numerical model relies on an optical micrograph observation to build a microstructure which takes into account the fibres and matrix distinction. The study focuses on the effects of laser incidence angle, fibre orientation and laser power on heat flux absorption by the microstructure and temperatures. Finally, a comparison with a standard and a more sophisticated 1D homogeneous model is carried out.

## 2. Method & Material

### *2.1. Thermo-optical microstructure model*

The thermo-optical model is based on the description of a single static tape laser heating at the micro-scale. To this end, a two-phase microstructure accounting for the fibres and matrix distinction is created and used as the input geometry to a FEM simulation. Then, a ray-tracing algorithm is developed to compute the laser absorption by the microstructure. Based on the absorption field, a simulation of heating and cooling phases is performed. Temperatures in the tape are extracted and analysed. Simulations are carried out under various configurations, *i.e* fibre orientations and laser incidence angles.

#### *2.1.1. Microstructure of the tape*

In order to compare experimental and numerical temperatures, the microstructure has to fit the fibre distribution of the experimental sample. To do so, a cross-section micrograph of an AS7/PEKK7002 [28, 29] tape is performed (Fig. 2(a)). The micrograph, chosen here as a representative picture of the

overall microstructure, points out the heterogeneity of fibre distribution in the thickness of the tape $e = 240\,\mu m$. Porosities and inclusions (remaining from the polishing process) are also visible.

Two methods were investigated to generate the most representative microstructure. The first method considered is based on automatic thresholding filters (Otsu [30], IsoData, ...) segmentation followed by a Hough's transform [31] which performs circular shape detection on a binary image. Fig. 3(a) points out the limits of this method for dense microstructures as close fibres are considered as one region which skews the microstructure identification. As a result, the average Fibre Volume Fraction (FVF) is substantially underestimated below 0.43.

A more sophisticated method has been investigated based on a segmentation with Weka [32]. This tool enables the segmentation of a grayscale image into several classes which makes it possible to split the pixels into fibre, matrix, porosities/inclusions and background groups. The tool is trained on micrographs by manually selecting the areas corresponding to the respective classes. As micrograph quality is high, less than 50 areas are sufficient for a precise identification of fibres and matrix.

From the segmented image (Fig. 3(b)), the average FVF is measured at 50%, which is close to the supplier datasheet. It exhibits a higher FVF close to the surfaces ($v_f > 55\%$) and a weaker fraction at core ($v_f \approx 40\%$). As the distribution is slightly asymmetric and the irradiated surface during the experiment can correspond either to the lower or upper surface, an artificial microstructure is generated with an average symmetric distribution with respect to the micrograph (Fig. 2(c)). The random generation process tries to fit at best these average features. The microstructure is divided into layers defined by their height and FVF. Each layer is generated by a method chosen according to the FVF. The first method, designed for higher FVF ($v_f > 49\%$), involves filling the layer rectangle with a hexagonal structure of circles. These are then slightly moved in random directions to remove the regularity of structure. The second method applies to lower FVF. A fine grid of the layer geometry is created from which a first circle is created at a random grid point position. Then, the next circle is created at the grid position which maximises the minimal distance to the previous circles and boundaries. The process is iteratively repeated until the required number of circles to obtain the FVF is reached. Additional random displacements of circles are computed after the layers have been assembled to smooth out interfaces.

The microstructure is then used to define the geometry and create the mesh. The fibre diameter corresponds to its nominal value 6.9 $\mu m$ confirmed by microscopy. A preliminary study of the Representative Elementary Volume (REV) was first carried out. It consisted of several laser heating

simulations on multiple widths with statistically identical microstructures. The obtained temperature converges for a minimal microstructure width: $l = 100\,\mu m$.

*2.1.2. Creation of geometry & mesh*

The mesh (Fig. 4(a)) is computed with GMSH [33]. To fit the experimental configuration, an air layer and the steel socle are added (see Sec. 2.2). Surfaces are extruded on one layer of length $h = 1.0\,\mu m$ giving tetrahedra elements with P1 interpolation. The nominal element characteristic length $l_c$ is set at 0.5 $\mu m$ and increases in the steel frame thickness. This value was chosen after a convergence study.

*2.1.3. Absorption of the laser heat flux*

Absorption of the laser heat flux is exclusively modeled by a surface heating condition in standard models. Here, the absorption of the laser flux by the microstructure relies on the hypothesis of PEKK transparency to the laser wavelength. Indeed, spectroscopy measurement performed highlighted the low absorptivity of PEKK material at the laser wavelength on samples that are few centimeters thick [21, 34]. PEKK, especially when crystallised, exhibits a semi-transparent nature, but its absorptivity on distances as small as some fibres' diameters ($\approx 20 - 30\,\mu m$) is negligible. As a result, the matrix is considered transparent on such distance. Consequently, the laser energy is only absorbed by the carbon fibres and transferred to the matrix by conduction. Some studies [21, 35] performed spectral reflectivity at similar laser wavelength on carbon fibres-reinforced thermoplastics and showed that the composite absorptivity depends on fibre orientation $\varphi$ and laser incidence angle $\theta$ (Fig. 5). Moreover, the maximal absorptivity in normal incidence has been measured around 0.9. Based on these observations, the carbon absorption coefficient $\alpha_{carbon}$ is fixed at $0.9 \pm 0.05$.

A ray-tracing algorithm was developed to compute the laser absorption by carbon fibres. It involves discretising very finely the laser beam

$$\overrightarrow{\phi_{laser}} = \phi_{laser}\,\overrightarrow{q} \tag{1}$$

where $\overrightarrow{q}$ is the unit direction vector of the laser flux and $\phi_{laser}$ the laser heat flux. A large amount of rays is required to ensure that every region of the heated fibres is detected by the algorithm. The intersection between the incident lines and the fibres is computed depending on fibre orientation $\varphi$ and laser incidence angle $\theta$. The laser flux vector $\overrightarrow{q}$ (Eq. A.4) is projected in the cross-section plane $(xy)$, resulting in a projected incidence angle $\eta$ (Eq. A.3) as illustrated in Fig. 6(a). An important feature is the computation of reflections until the total energy absorption or reflection to the outer medium. The

algorithm, described in Appendix A, is computed in Matlab R2021a for analytical cylinders. Fig. 7 draws the intersection of the incident laser flux with the fibres for a normal incidence $\theta = 0°$. The ray-tracing code outputs the laser absorption field $\alpha$ as a function of space, as illustrated in Fig. 7(b). The absorption field is then integrated over the surface of heated elements (Fig. 6(b)(c)) such as:

$$\alpha_{elem} = \frac{1}{S_{elem}} \iint_{S_{elem}} \alpha \, dS \tag{2}$$

where $\alpha_{elem}$ is the element absorption value, $S_{elem}$ is the element surface. Large elements lead to an overestimation of the global absorption as a same point can be projected on two elements. Finally, the element-discretised absorption field $\alpha_{elem}$ applied at each element barycenter is interpolated on the mesh nodes by taking the average value of adjacent elements. This last step could be improved by weighting the node values with the distances to element barycenters. Nonetheless, the obtained discrete absorption field $\alpha_{node}$ should be overall barely affected.

*2.1.4. Thermal simulation of heating and cooling phases*

The simulation of the heating and cooling phases is computed with Freefem++ [36]. The boundary value problem is illustrated in Fig. 4(b). The heat equation is solved in four physical volumes: fibres, matrix, steel as well as in the air gap between the tapes and the steel part. Temperature field T, is submitted to the following equations set:

$$\forall t > 0 \begin{cases} \rho C_p \dfrac{\partial T}{\partial t} - div(\overline{\overline{k}}.\overrightarrow{\nabla} T) = Q_v, \quad \forall x \in V_i,\ i \in \{mat, f, air, steel\} \\ \overrightarrow{\phi} \cdot \overrightarrow{n} = 0, \quad \forall x \in S_{lat} \\ T = T_{amb} = 20°, \quad \forall x \in S_{steel,inf} \\ \phi = h_{air}(T - T_{amb}), \quad \forall x \in S_{mat,top} \\ \phi = \alpha \phi_{laser}, \quad \forall x \in S_{hf},\ \forall t < t_{heat} \end{cases} \tag{3}$$

where $\rho$ is the material density, $C_p$ the specific heat capacity, $\overline{\overline{k}}$ the conductivity tensor, $Q_v$ the volumetric heat. $\overrightarrow{n}$ is the outer normal vector to the 2D heated element and $\overrightarrow{\phi}$ the heat flux. The air convection coefficient is $h_{air} = 5\, W.m^{-2}.K^{-1}$. Surface $S_{steel,inf}$, $S_{mat,top}$, $S_{lat}$ and $S_{hf}$ are respectively the steel back surface, matrix upper surface, the sides, front and rear surfaces, and the heated fibres surfaces. $V_i$ is the volume of material $i$. Vector $\overrightarrow{q}$ is the resulting direction vector of laser heat flux (Eq. 1), depending on tape orientation $\varphi$ and incidence angle $\theta$, such as:

$$\overrightarrow{q} = \begin{pmatrix} -\sin\theta \sin\varphi & -\cos\theta & -\sin\theta\cos\varphi \end{pmatrix}^T \tag{4}$$

Heating time $t_{heat}$ was fixed at 20 ms for all simulations, in accordance with experimental conditions described further, and corresponds approximately to the exposure time in a manufacturing process context at a 500 $mm.s^{-1}$ laying speed with a 12 $mm$ laser beam width. The time is supposedly inferior to the heat diffusion time from the front to the back surface of the ply. Consequently, the back surface condition does not affect heat transfers during the heating phase. This hypothesis is based on the computation of penetration time $t_p$ in a semi-infinite model [37], such as:

$$t_p = \frac{e^2}{8\alpha_{diff}} \tag{5}$$

where $\alpha_{diff} = \dfrac{k_{comp,TRA}}{\rho_{comp} C_{p,comp}} \approx 4\ 10^{-7}\, m^2.s^{-1}$ is the composite transverse diffusivity, $e$ the ply thickness and $k_{comp,TRA}$, $\rho_{comp}$, $C_{p,comp}$ respectively the transverse thermal conductivity, density and specific heat capacity of the composite laminate.

It leads to an approximate 20 ms penetration time which is verified in Sec. 3.2. 50 iterations with a 0.8 ms time step are performed to precisely describe the heating and cooling kinetics with a total simulation time of 40 ms.

### *2.2. Experimental set-up*

The core of the set-up is a metallic bench on which a rotating 2kW laser diode LDM 200 - 6000 is mounted (Fig. 8). A composite tape is held onto the metallic support to be irradiated by the laser diode at a 980 $nm$ wavelength with controlled time and power. The distance and the incidence angle of the laser optics with regards to the tape surface can be adjusted, respectively from 150 to 200 $mm$ and 15° to 75°. The bench itself is equipped with a heating resistive wire and instrumented with thermocouples and a small response time heat flux sensor [38]. Above the support, a FLIR XC609 IR camera monitors the evolution of temperature at the composite surface. Laser heat flux was calibrated at several working distances with the help of the heat flux sensor. The sensor is composed of three thermocouples with 50 $\mu m$ wires welded in the thickness below the surface. The evolution with time of an incoming heat flux irradiating the sensor surface is calculated with the Beck inverse method [39] supplied with the thermocouples responses whose locations are perfectly known. The usual algorithm was modified to retrieve the thermocouples response time [38]. As a result, the experimental laser heat flux is known and used as the input laser heat flux in the simulation. Fig. 9 displays the thermographs of surface temperature at the end of the heating phase for a fibre orientation $\varphi = 0°$. The projection of the laser beam on the tape surface leads to a larger heated area in grazing incidence (Fig. 9)(d)). Moreover, the tape surface heterogeneity is visible from the color contrast. In order to track the

average temperature evolution in time, the surface temperature is averaged over a thin red box (50 $\times$ 5 pixels$^2$) which corresponds to the center of the heated area on which the heat flux is calibrated. Repeatability tests were carried out on 5 samples for each configuration. The resulting experimental uncertainty is about 2% including the tapes' heterogeneity and the accuracy error of the measurement process. These experimental surface temperatures are compared to numerical ones in Sec. 3.2.

### *2.3. Material properties*

Heat equation (Eq. 3) is solved in each material which requires a precise knowledge of their properties: density, thermal conductivity and specific heat capacity. Properties are summarized in Tab. 1. Carbon fibre AS7 $\rho_f$ and PEKK7002 $\rho_m$ densities are set thermally constant [28, 29] as their variations are considered low on the studied temperature range ($\approx 20 - 250°C$). Their respective specific heat capacity $C_{p,f}$ and $C_{p,m}$ were measured by Differential Scanning Calorimetry (DSC) TA Q200. Thermal conductivities were measured using a Guarded Hot Plate (GHP) method [40]. From Fourier's law,

$$\phi_l = k\left(\frac{T_2 - T_1}{e_l}\right) \tag{6}$$

thermal conductivity $k$ is determined knowing the laminate thickness $e_l$, $T_1$ and $T_2$ the cold and hot temperatures and $\phi_l$ the heat flux passing through the laminate.

The matrix thermal conductivity was measured at room temperature on a PEKK7002 plate as $k_m = 0.27\,W.m^{-1}.K^{-1}$ with a maximal $\pm 5\%$ measurement uncertainty. Owing to their manufacturing process and geometry, PAN-type carbon fibres' thermal behavior is anisotropic [23]. The heat spreads quicker in the fibre direction so that the longitudinal thermal conductivity is higher than the transverse (radial) thermal conductivity. Based on literature, PAN-type carbon fibres' longitudinal thermal conductivity ranges between approximately 7.0 and 10.3 $W.m^{-1}.K^{-1}$ [23, 41] whereas transverse thermal conductivity is estimated between 0.5 and 3.5 $W.m^{-1}.K^{-1}$ [23, 42]. As the heat transfer is mainly one-dimensional in the depth direction in our configuration, transverse thermal conductivity is the most relevant parameter to identify accurately. The longitudinal thermal conductivity $k_{f,LONG}$ used in the simulation is fixed at 10 $W.m^{-1}.K^{-1}$[41]. This value barely influences the heat transfer in comparison with the transverse conductivity.

To skirt the difficulty of carbon fibre radial thermal conductivity measurement due to their size, an inverse method based on a GHP measurement is used. First, a transverse conductivity measurement is performed on 6 samples of a 24-ply unidirectional plate with an effective thickness of 4.6 $mm$. The average composite transverse thermal conductivity is estimated: $k^{exp}_{comp,TRA} = 0.69\,W.m^{-1}.K^{-1}$ with

a variability of ±1.7%. The inverse method then consists of running a FEM simulation on a RVE of the plate microstructure with different values of fibre transverse thermal conductivity until it fits this macroscopic measurement. To do so, a micrograph of the composite plate is performed with an average FVF measured at 54.1%. Using the methodology described in Sec. 2.1.1, a representative microstructure of fibre distribution in matrix is generated and meshed. To verify the convergence of the solution, the simulation was performed with several microstructure sizes. The optimal RVE size was found to be a rectangular zoom of height 900 $\mu m$ and width 100 $\mu m$. The simulation consists of a steady state model considering the cold and hot surface temperatures with adiabatic conditions on the lateral sides. The heat flow $\phi_{comp}$ through the plate thickness is averaged to compute the equivalent transverse thermal conductivity of the plate $k^{num}_{comp,TRA}$ using Eq. 6 and the microstructure thickness. Rayleigh, Charles-Wilson and Maxwell models' curves were added with the same FVF. Their respective expressions for the homogenised transverse thermal conductivity [24–27, 43] are noted hereunder:

$$k^{Ray}_{comp,TRA} = k_m \left( 1 + \frac{2v_f}{\frac{k_m + k_{f,TRA}}{k_m - k_{f,TRA}} - v_f + \frac{k_m - k_{f,TRA}}{k_m + k_{f,TRA}}(0.306v_f^4 + 0.0134v_f^8)} \right) \tag{7}$$

$$k^{CW}_{comp,TRA} = k_m \left( \frac{k_{f,TRA}(1+v_f) + k_m(1-v_f)}{k_{f,TRA}(1-v_f) + k_m(1+v_f)} \right) \tag{8}$$

$$k^{Max}_{comp,TRA} = k_m \left( \frac{k_{f,TRA} + 2k_m + 2v_f(k_{f,TRA} - k_m)}{k_{f,TRA} + 2k_m - v_f(k_{f,TRA} - k_m)} \right) \tag{9}$$

where $k_m$ is the matrix thermal conductivity, $v_f$ the fibre volume fraction and $k_{f,TRA}$ the fibre transverse thermal conductivity.

Results for different values of $k_{f,TRA}$ and $v_f$ are plotted in Fig. 10(a) together with the three classical analytical models described above. The actual fibre transverse thermal conductivity minimizes the difference between microstructure simulation curve (blue plain line) and the experimental homogeneous transverse thermal conductivity (black dashed line) such as: $k_{f,TRA} = 2.2\ W.m^{-1}.K^{-1}$. Moreover, the microstructure simulation is in accordance with Charles-Wilson and Rayleigh models.

As the micrograph binarisation leads to FVF uncertainty, fibre transverse thermal conductivity sensitivity was also studied and compared to Charles-Wilson and Rayleigh models (Fig. 10(b)). Both literature models and microstructure simulation highlight the sensitivity to FVF, especially for a big difference of conductivity between matrix and fibre. For example, a ±5% FVF uncertainty leads to a fibre transverse thermal conductivity range from 1.7 to 5.0 $W.m^{-1}.K^{-1}$. This result points out the necessity to properly identify the FVF. The PEKK thermal conductivity [44] barely varies on

the studied temperature range up to 250° and the slight increase of transverse composites thermal conductivities is mainly caused by microstructure changes (compaction and decrease of void fraction). Therefore, matrix and carbon fibre thermal conductivities are set constant.

## 3. Results & Discussion

### *3.1. Heat absorption*

The ray-tracing algorithm computes the absorption of the laser beam from the incident rays to the $N_{refl}$ reflections until the input power $P_{inc,tot}$ is either absorbed by the microstructure $P_{abs,tot}$ or reflected to the environment $P_{refl,tot}$. These values are then used to compute the equivalent absorptivity $\alpha_{eq}$ and reflectivity $\rho_{eq} = 1 - \alpha_{eq}$ of the composite such as:

$$\alpha_{eq} = \frac{P_{abs,tot}}{P_{inc,tot}} \tag{10}$$

For the sake of representativity and numerical efficiency, the calculations analyzed hereafter were performed on randomly generated microstructures (see Fig. 2(b)) containing 320 fibres and for a numerical FEM model of 260 000 nodes. The temperature variability has been shown negligible over 10 randomly generated microstructures exhibiting a similar fibre distribution through the thickness.

As can be seen from Fig. 11, the absorptivity strongly decreases at grazing incidence angles with no effect on fibre orientation and follows a cosine function. Therefore, the required laser power is higher to compensate the decrease of laser absorption in order to supply an equivalent amount of energy to the tape. The second information extracted from the ray-tracing algorithm is the distribution of the laser flux absorption through the thickness of the tape $q_\alpha$.

$$q_\alpha(y) = \frac{1}{\alpha_{tot}} \sum \alpha \left( y - \frac{\Delta y}{2} \leq y < y + \frac{\Delta y}{2} \right), \quad 0 < y < e \tag{11}$$

with $\Delta y = 0.2\,\mu m$ the discretisation step and $\alpha_{tot} = \sum_i^N \alpha_i$ the total absorption computed on the absorption field $\alpha$ described by $N$ points.

The distribution is plotted in Fig. 12(a) for $\varphi = 0°$ and $\theta = 15°$ and characterized by a double-peak distribution describing the absorption of the laser heat flux by the two first rows of fibres. As a result, the flux is fully absorbed at a depth of 10 $\mu m$ which is caused by the high FVF close to the surface.

The distribution is then properly fitted with a double-beta distribution $db(y)$ such as:

$$db(y) = b(y, a_1, b_1, k_1) + b(y, a_2, b_2, k_2) \tag{12}$$

$$b(y, a, b, k) = \frac{k}{\beta(a, b)} \left(\frac{y}{e}\right)^{a-1} \left(1 - \frac{y}{e}\right)^{b-1} \tag{13}$$

$$\beta(a, b) = \int_0^1 t^{a-1}(1-t)^{b-1} dt \tag{14}$$

In the grazing incidence configuration with a 90° fibre orientation, the first peak shifts closer to the surface and the second peak vanishes (Fig. 12(b)). In this configuration, the laser beam mainly intersects the top of the first row of fibres. This trend is confirmed with the absorption depths at 50% and 100% plotted in Fig. 12(c). The first thing that can be noticed is that the incidence angle has no effect on 0° fibre orientation as the same fibres are heated for every incidence angle. Another detail is that a small increase in absorption depth can be observed from 0 to 30° incidence and is followed by a strong decrease for more grazing incidences when the fibre orientation differs from 0°, meaning that the absorption is overall closer to the tape surface.

To sum up the heat absorption results, the absorptivity of the composite is only affected by the incidence angle with lower values in grazing incidences whereas the volumetric absorption distribution (shape and depth) depends on both the fibre orientation and the incidence angle.

*3.2. Comparison of experimental and numerical results*

Temperature and heat flux are extracted at every iteration. Fig. 13 shows the distribution of temperature and heat flux through the thickness of the tape in a near-normal incidence at three time steps: beginning and end of heating phase and end of cooling phase. At the end of the heating phase, temperature has substantially increased in the first half of the tape whereas the lower surface is barely impacted. It then homogenizes during the cooling. Fibre contours are slightly visible and point out the diffusion time from fibres to matrix due to high thermal conductivity differences. The heat flux distribution clearly highlights the percolation paths passing from fibre to fibre where heat diffusion through the thickness is facilitated.

The temperature is then homogenised within fibres and matrix through the thickness of the tape (Fig. 14). After 1 ms, the temperature has increased only in the first 50 $\mu m$ which is due to the low volumetric absorption depth. The maximal surface temperature is reached at the end of heating whereas the back surface temperature has barely increased which confirms the validity of the assumption that the penetration time is higher than 20 ms. As observed graphically, temperature distribution becomes more homogeneous at the end of the cooling phase.

The temperature is finally averaged over the upper surface and compared to the experimental one (Fig. 15). The orange line and span respectively correspond to the mean and standard deviation (experimental uncertainty) values obtained from 5 samples' measurements which highlight the material and temperature measurement variability. In order to work in the same calibration range of the camera in every configuration and reach a similar maximal temperature around 200°C which avoids melting of thermoplastic, the laser power was substantially increased for grazing incidences. Indeed, the experimental laser heat flux in near-normal and grazing incidence are set respectively at 1.4 and 2.66 $MW.m^{-2}$ with a 5% uncertainty. This observation confirms the high decrease of absorptivity pointed out in Sec. 3.1. An initial piece of information worth knowing is the negligible effect of fibre orientation on the experimental temperatures in both near-normal and grazing incidences as a similar temperature evolution is observed for the three fibre orientations. The numerical laser heat flux has been determined by minimizing the residuals between numerical and experimental surface temperatures. The respective values in near-normal and grazing incidences are 1.47 and 2.793 $MW.m^{-2}$, corresponding to a 5% correction. As a result, the optimal numerical laser heat flux is within the experimental laser flux uncertainty in every configuration. Therefore, the evolution in experimental temperatures is overall precisely fitted by the model. As the simulation is dependent on multiple parameters, sensitivity to the material properties and microstructure variability are studied.

### *3.3. Sensitivity analysis*

#### *3.3.1. Uncertainty of material properties*

First, sensitivity to the material properties is evaluated. From Sec. 2.3, PEKK thermal conductivity uncertainty is directly given by GHP measurement: $k_m = 0.27 \pm 0.0135\ W.m^{-1}.K^{-1}$. This uncertainty is used for the non-linear identification of carbon fibre transverse thermal conductivity uncertainty from Fig. 10, such as $k_{f,TRA} \in [1.9, 2.70]\ W.m^{-1}.K^{-1}$. The surface temperature is not substantially affected as it leads to a maximal temperature gap of 2°C. The effect of carbon fibre absorption coefficient uncertainty has also been estimated such as $\alpha_{carbon} = 0.9 \pm 0.05$ leading to a 9°C surface temperature variation.

#### *3.3.2. Microstructure variability*

The effect of microstructure variability was also studied with simulations on a different material characterised by a lower (41%) FVF (Fig. 16). Based on the method described in Sec. 2.1.1, an artificial microstructure with a similar FVF distribution was created. The analysis of heat absorption points out that the total absorption depths are noticeably higher for this material, from 5 to 30 $\mu m$, compared

to the reference material between 3 and 13 $\mu m$. Surface temperature comparison (Fig. 17) points out a light modification of heating and cooling kinetics. Indeed, in near-normal incidence, surface temperature increases faster in the first 10 ms for the denser microstructure as the laser absorption is closer to the surface. After this period, surface temperature of the scattered microstructure becomes higher which is due to the higher proportion of matrix slowing the heat diffusion (lower thermal conductivity). Likewise, cooling is also slower with a scattered microstructure. The kinetics trend is similar in grazing incidence. However, the maximal surface temperature is slightly higher for $v_f = 0.41$, up to 12°C increase. This is due to a larger absorptivity (2-4%) and a deeper absorption length combined with a lower diffusivity. Moreover, the effect of fibre orientation is noticeable with a 10 °C higher temperature at 90° fibre orientation with respect to 0°.

These results underline that the microstructure density and fibre distribution perceptibly affect laser energy absorption and temperature evolution in a complex manner. While scattering fibres promotes deeper heat penetration and a larger heated volume, promoting slower heating and cooling, depending on fibres' conductivity, the decrease of diffusivity can lead to higher temperatures. Precise knowledge of the prepreg microstructure is necessary to master the temperature field through the industrial AFP process. It is now clear that no simple rule of thumb can be deduced.

### *3.4. Comparison with 1D homogenised models*

As the state of the art points out, most composites models use 1D homogenised material whose properties are calculated by a given mixture rule, assuming values of fibres and matrix properties. Moreover, the absorption of laser beam energy is assumed to be surfacic. The pertinence of the microstructure model is assessed by comparing the surface temperature with this standard model. Based on these results, a more sophisticated homogenised 1D model can be defined by considering a volumetric absorption which follows the fitted double-beta distribution presented in Sec. 3.1. For both surface and volumetric homogenised models, the composite density $\rho_{comp}$ and specific heat capacity $C_{p,comp}$ are determined with a standard mixture law (Eq. 15) and the thermal conductivity follows the Charles-Wilson model (Eq. 8) that was proven to give the best agreement with our microstructure model. These values are calculated with a uniform fibre fraction. Simulations with homogenised properties which vary through the thickness depending on fibre fraction were performed and very slightly improved the approximation of temperatures compared with a uniform fibre fraction.

$$\rho_{comp}\, C_{p,comp} = v_f\, \rho_f\, C_{p,f} + (1 - v_f)\, \rho_m\, C_{p,m} \tag{15}$$

The surface heat flux condition $\phi_{surf}$ and volumetric heat source condition $Q_{vol}(y)$ (following Eq. 12) are respectively determined using the total absorption $\alpha_{abs,tot}$:

$$\phi_{surf} = \alpha_{abs,tot}\, \phi_{laser} \tag{16}$$

$$Q_{vol}(y) = \alpha_{abs,tot} \frac{\phi_{laser}}{\Delta y} db(y) \tag{17}$$

Fig. 18(a) compares the surface temperature evolution in near-normal incidence at 0° fibre orientation of the microstructure and 1D homogenised models with surface and volumetric heat source condition on the reference microstructure ($v_f = 0.50$). Whereas the surfacic model widely overestimates the microstructure model surface temperature up to 11°C, the volumetric condition leads to a precise approximation with a 3°C overestimation at the end of heating phase.

The study is then carried out in different configurations: near-normal and grazing incidences, dense and scattered microstructure (Fig. 18(b)(c)). The error of surface temperature at the end of heating phase is analysed for both surface and volumetric models with respect to the microstructure model. In every configuration, the volumetric heat source model reduces the error in comparison with the surfacic one. Moreover, the surface model leads to a greater error, up to 24°C, with a scattered microstructure due to the deeper absorption length. The error decreases slightly in grazing incidence as the absorption length lowers. As a result, the surface heat condition model does not provide an accurate estimation of the surface temperature. It is worth remembering that simulations were performed at 200 °C. Nevertheless, at the processing temperature of the AFP process, which is about 400°C, the absolute error is of course expected to be much higher.

These results show that the complex and time consuming simulations at the fibres scale can be replaced by a conventional homogenised continuous model, provided that a fine description of the volumetric heat flux absorption is used. The latter can be obtained by the thermo-optical model proposed here and is likely to be dependent on both the incidence angle and the fibre orientation, in some cases.

## 4. Conclusion

A thermo-optical model at the micro-scale of static tape laser heating is developed based on a ray-tracing algorithm. The model is designed to take into consideration microstructure variability and works with a thin RVE microstructure randomly generated which represents the fibre distribution through the thickness of the tape and was proved to be representative of the average behaviour of

the tapes. The numerical process enables the identification of a volumetric laser flux absorption which differs from the standard surface absorption model. The absorption shape depends on fibre orientation, incidence angle and the material microstructure, *i.e* FVF distribution. The algorithm makes it possible to compute equivalent absorptivity which decreases as the incidence angle increases. This new model enables us to precisely fit the evolution of experimental surface temperatures in every configuration studied. The volumetric absorption is then implemented in a 1D continuous equivalent model which homogenises fibre and matrix properties. A comparison with standard surface heating models highlighted the pertinence and accuracy of a volumetric heat source, thus opening the way to better temperature predictions in the AFP process, which is also proved to be strongly affected by fibre distribution.

Further developments include the use of this model in process configuration considering substrate and laying tape reflections. Another perspective is the design optimization of FVF distribution in the thickness of the tape to optimize the heat diffusion during the laying process.

**Acknowledgements**

This research work has been carried out in the scope of HAICoPAS consortium (Hexcel Composites, Arkema, Coriolis, Institut de Soudure, PEI, Ingecal, UMR CNRS: ENSAM-PIMM UMR 8006 and Nantes Université-LTeN UMR 6607), a PSPC project (projet de recherche et développement structurant pour la compétitivité) funded by BPI France.

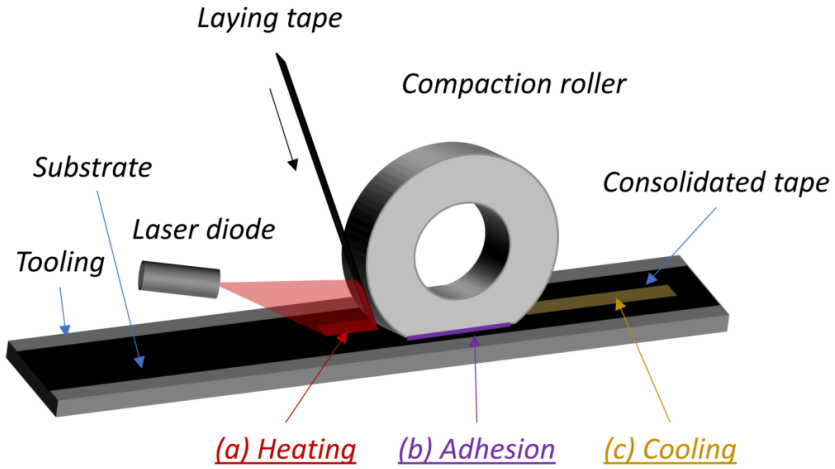


Fig. 1: Laser-assisted AFP process: (a) heating, (b) adhesion and (c) cooling.

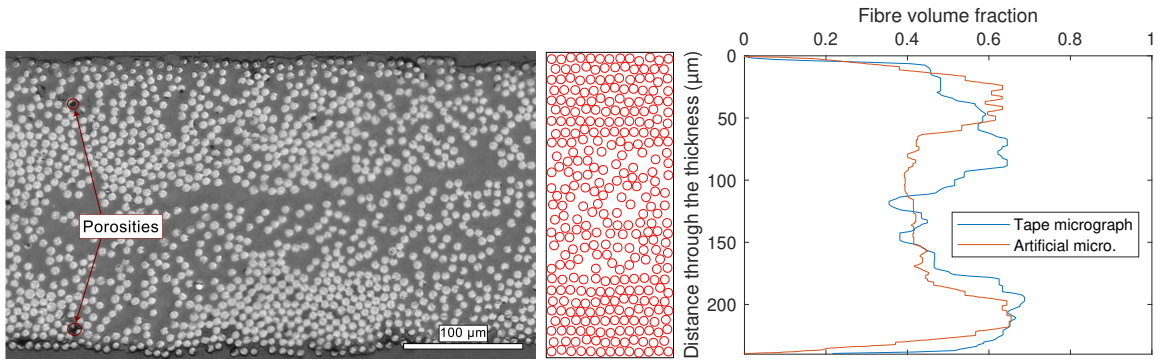


(a) (b) (c)

Fig. 2: (a) Tape micrograph (b) Random generated microstructure (c) Fibre volume fraction distribution through the thickness.

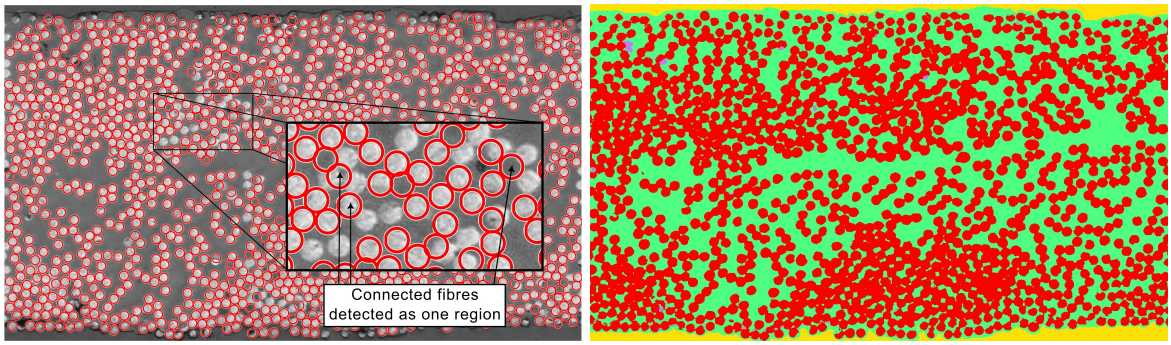


(a) (b) Resulting segmented image.

Fig. 3: Fibres identification with (a) Hough's transform method (b) Weka deep learning tool: fibres (red), matrix (green), porosities/inclusions (purple) and background (yellow).

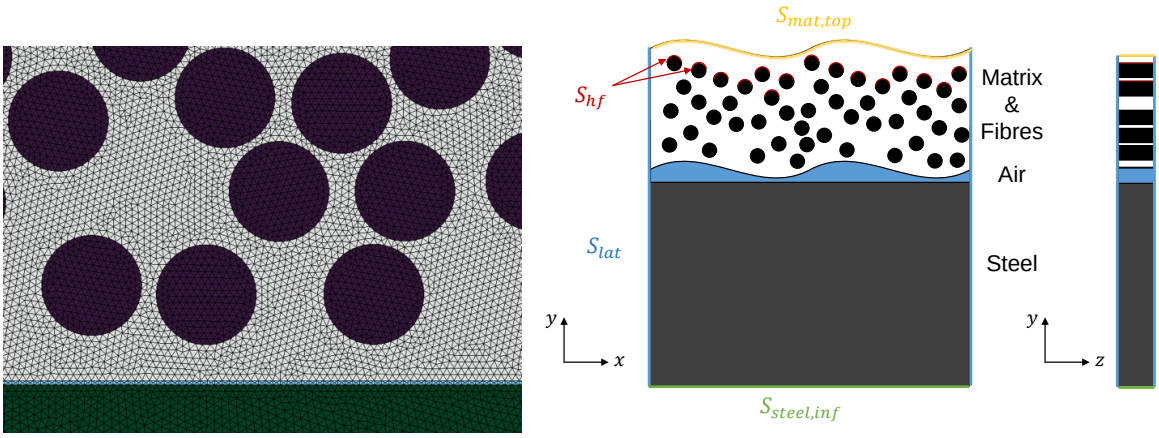


(a) (b)

Fig. 4: (a) Mesh: fibres (black), matrix (light gray), steel (green) and air (blue). (b) Schematic of the problem: volume and boundary conditions.

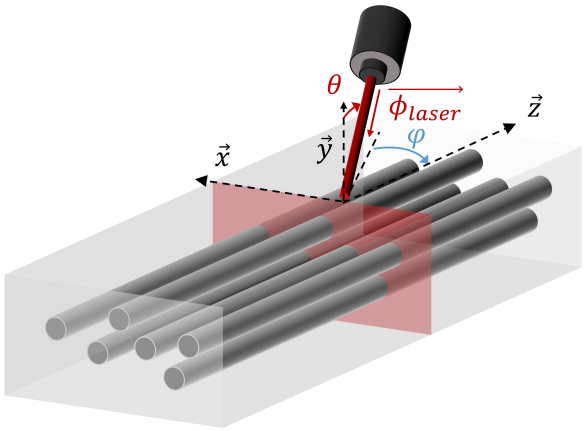


Fig. 5: Angular configuration of the laser heating.

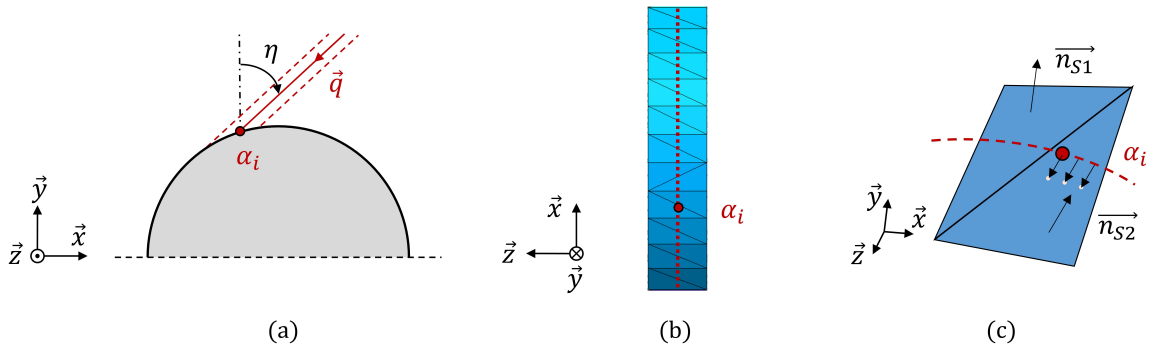


Fig. 6: Computational principle of (a) a ray oriented in $\vec{q}$ direction, intersecting a carbon fibre. (b) The near-analytical field $\alpha$ is set at the middle coordinate of layer along $\vec{z}$ axis. (c) As fibre elements, by definition, do not perfectly fit the analytical cylinder contour, the absorption field points are projected onto the fibres surface elements.

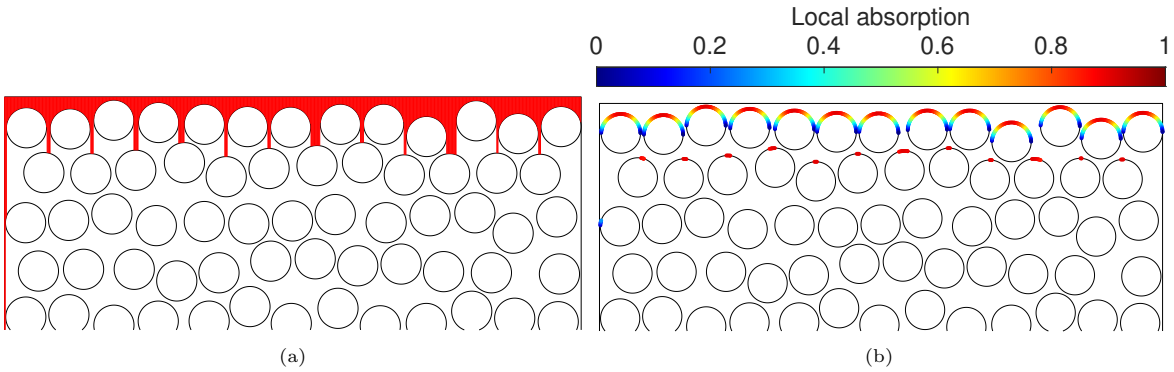


Fig. 7: Illustration of the results of the ray-tracing algorithm in normal incidence: $\theta = 0°$ (a) intersection of laser incident beam with carbon fibres (b) resulting absorption field $\alpha$.

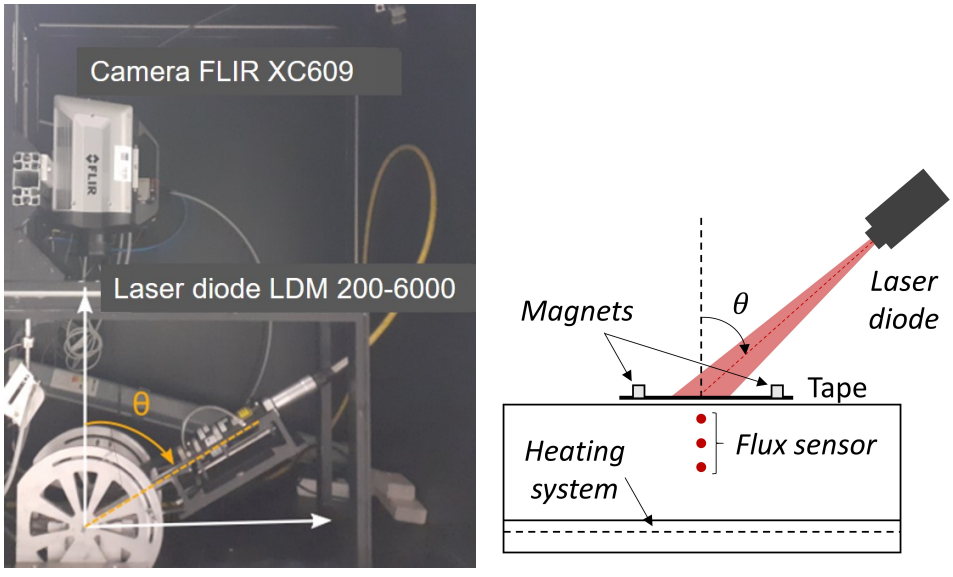


Fig. 8: Experimental bench: (a) a laser diode heats up the tape surface with a controlled incidence angle and an infrared camera measures the tape surface temperature with normal incidence. (b) Schematic of the instrumented bench.

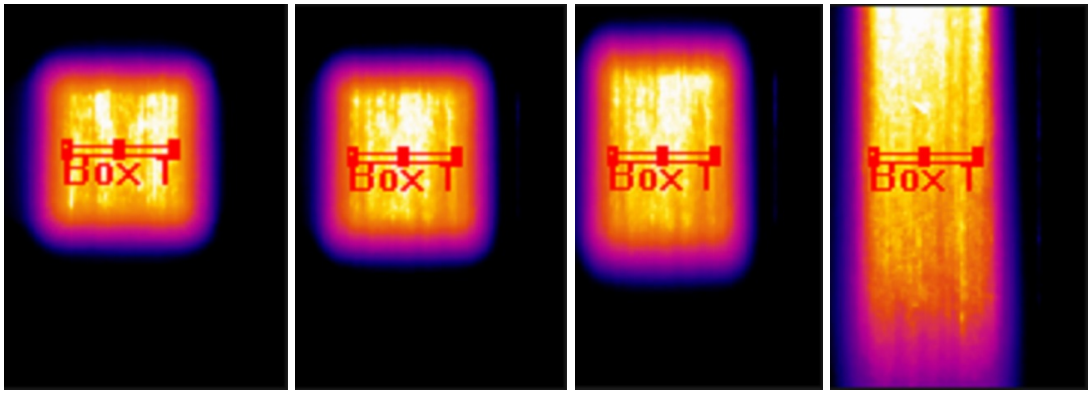

(a) $\theta = 15°$. (b) $\theta = 30°$. (c) $\theta = 45°$. (d) $\theta = 75°$.

Fig. 9: Thermographs of surface temperature at the end of the heating phase $t = 20\,ms$ for increasing incidence angles and fibres orientation $\varphi = 0°$.

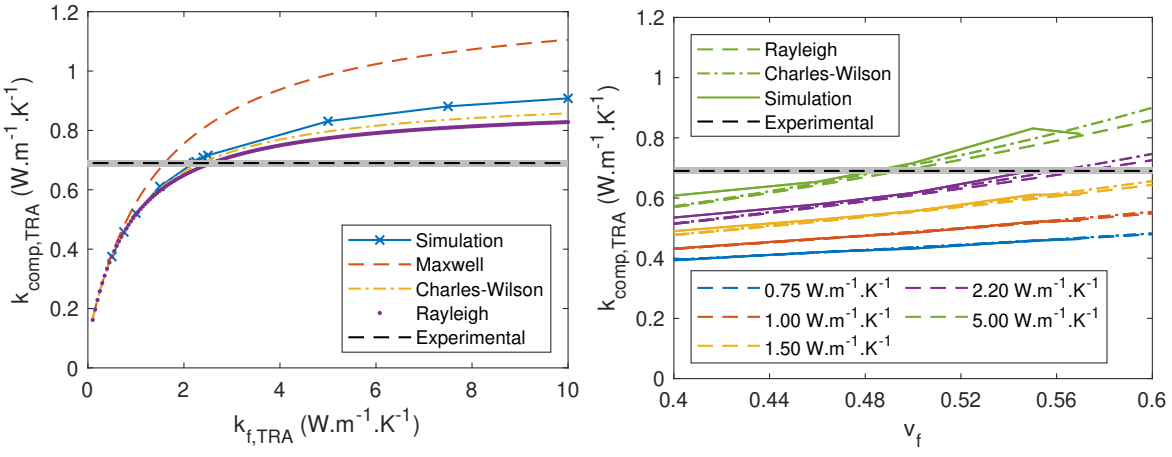


(a) (b)

Fig. 10: Identification of the fibre transverse conductivity $k_{f,TRA}$ through a sensitivity analysis: (a) homogenised thermal conductivity evolution with $k_{f,TRA}$ according to different approaches and (b) homogenised thermal conductivity evolution with the FVF for different values of $k_{f,TRA}$.

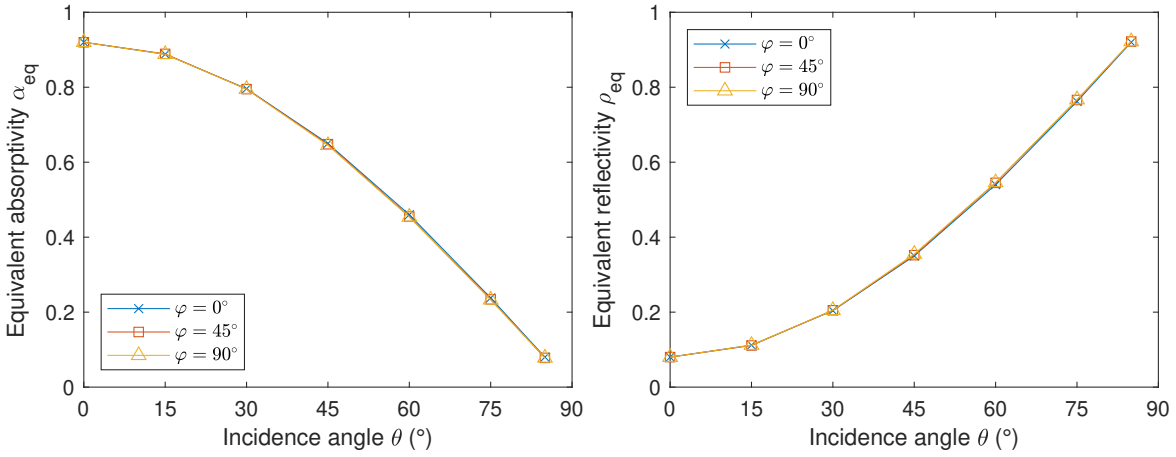


(a) (b)

Fig. 11: Computed optical properties of the tape at the macroscopic scale: (a) equivalent absorptivity and (b) reflectivity of the microstructure for three fibre orientations: 0, 45 and 90°.

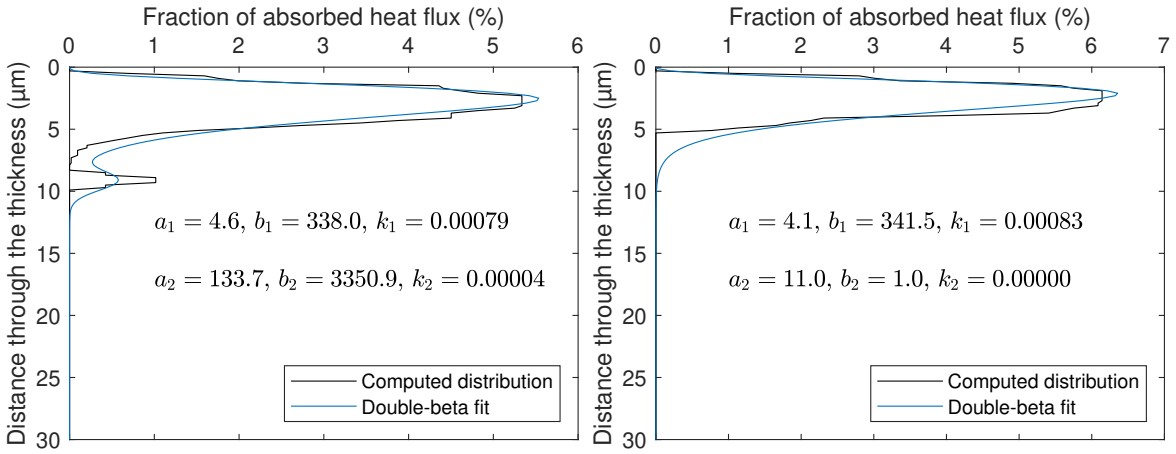


(a) Near-normal incidence: $\varphi = 0°$, $\theta = 15°$ (b) Grazing incidence: $\varphi = 90°$, $\theta = 60°$

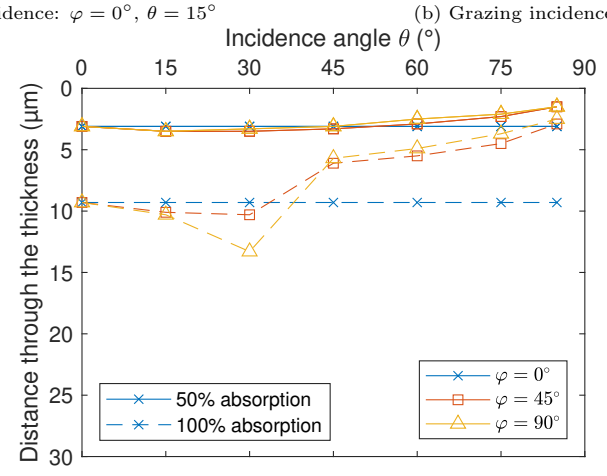


(c) Grazing incidence: $\varphi = 90°$, $\theta = 60°$

Fig. 12: (a) (b) Distribution of the volumetric absorption through the thickness fitted by a double-beta distribution. (c) Absorption depths at 50% (−) and 100% (−−) against incidence angle for 0, 45 and 90° fibre orientation.

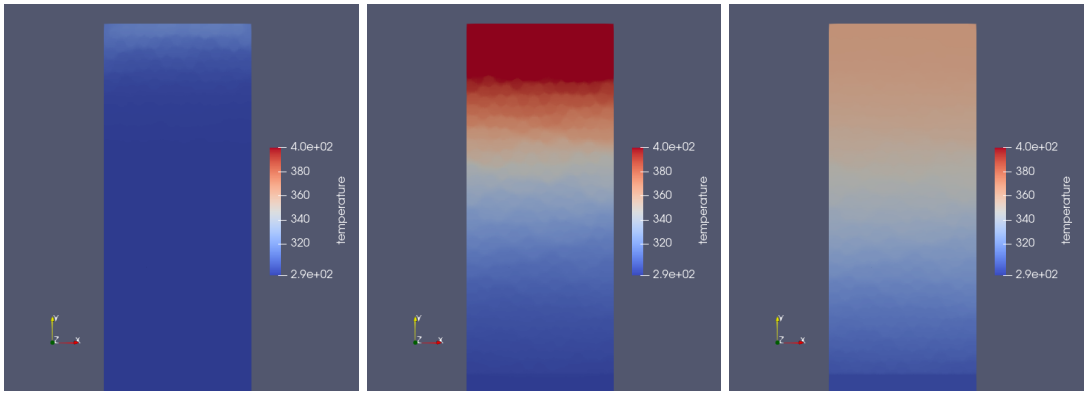


(a) $t = 0.8\,ms$ (b) $t = 20\,ms$ (c) $t = 40\,ms$

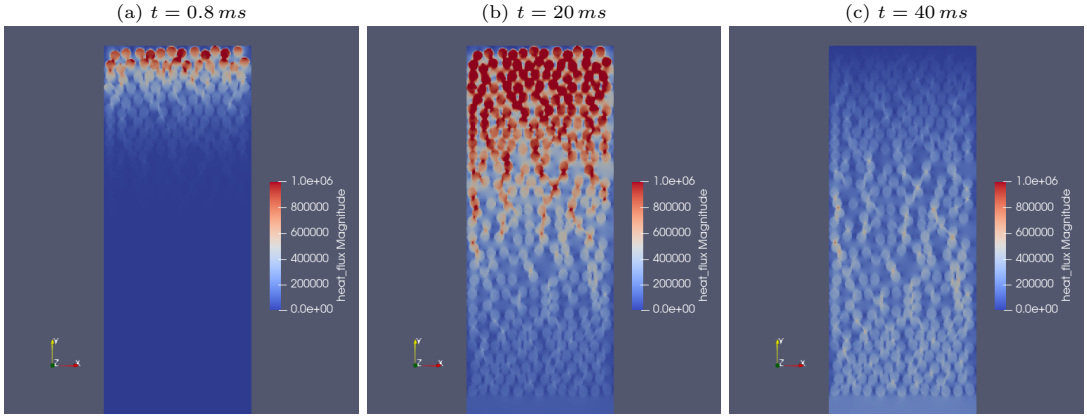


(d) $t = 0.8\,ms$ (e) $t = 20\,ms$ (f) $t = 40\,ms$

Fig. 13: Distribution of (a) (b) (c) temperature ($K$) and (d) (e) (f) heat flux ($W.m^{-2}$) in near-normal incidence at (a) (d) beginning $t = 0.8\,ms$ (b) (e) end of heating $t = 20\,ms$ and (c) (f) end of cooling $t = 40\,ms$.

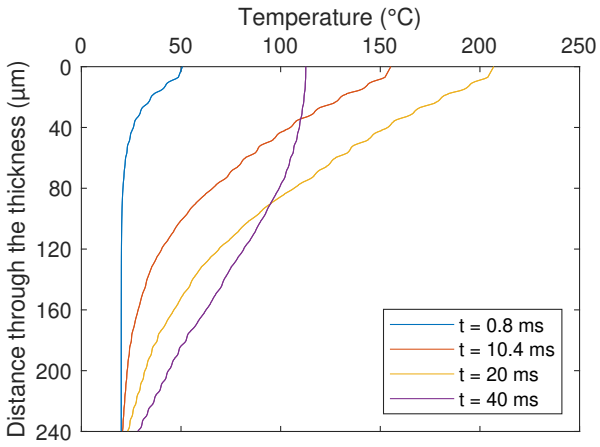


Fig. 14: Distribution of temperature in near-normal incidence through the tape thickness at different times: beginning, middle and end of the heating phase, and end of the cooling phase.

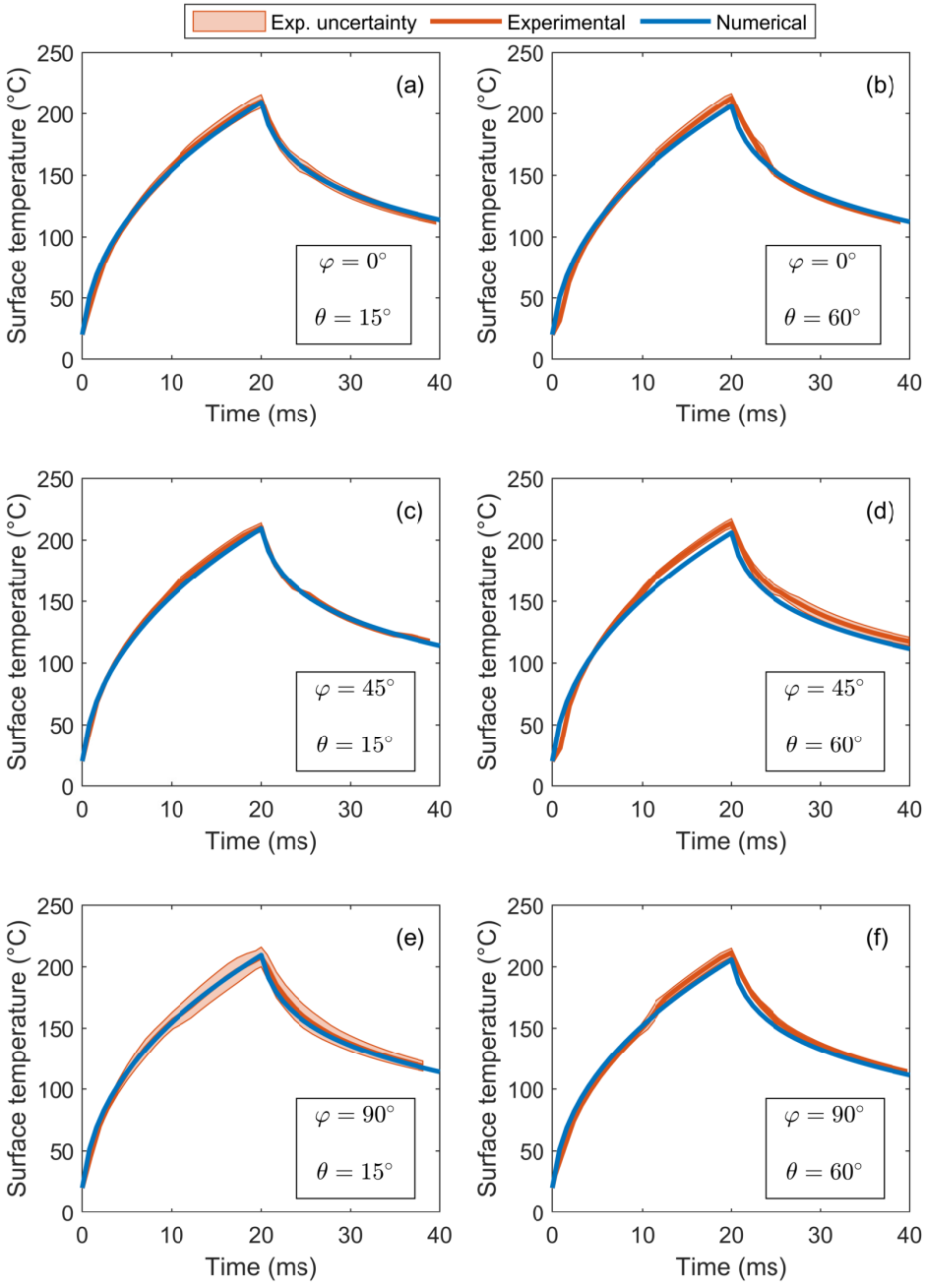


Fig. 15: Evolution of numerical and experimental surface temperature for (a) (c) (e) near-normal $\theta = 15°$ and (b) (d) (f) grazing $\theta = 60°$ incidences with (a) (b) $\varphi = 0°$ (c) (d) and $\varphi = 45°$ (e) (f) $\varphi = 90°$. The experimental and numerical laser heat flux in near-normal and grazing incidence are respectively 1.4 and 2.66 $MW.m^{-2}$, and 1.47 and 2.793 $MW.m^{-2}$.

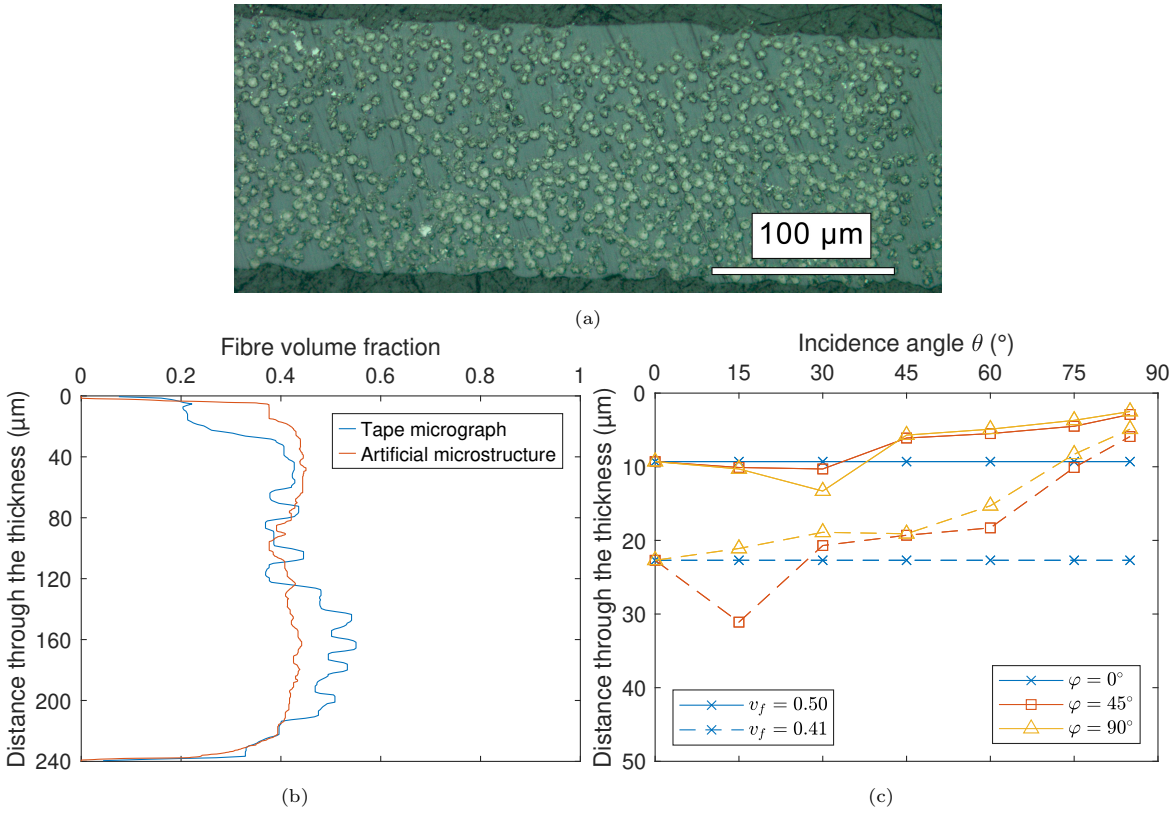


Fig. 16: CF/PEKK material with scattered fibres: lower FVF and deeper heat flux absorption (a) Tape cross-section micrograph (b) Fibre volume fraction distribution of tape micrograph and artificial microstructure (c) Total absorption depths against incidence angle for the reference ($v_f = 0.50$) and scattered microstructure ($v_f = 0.41$).

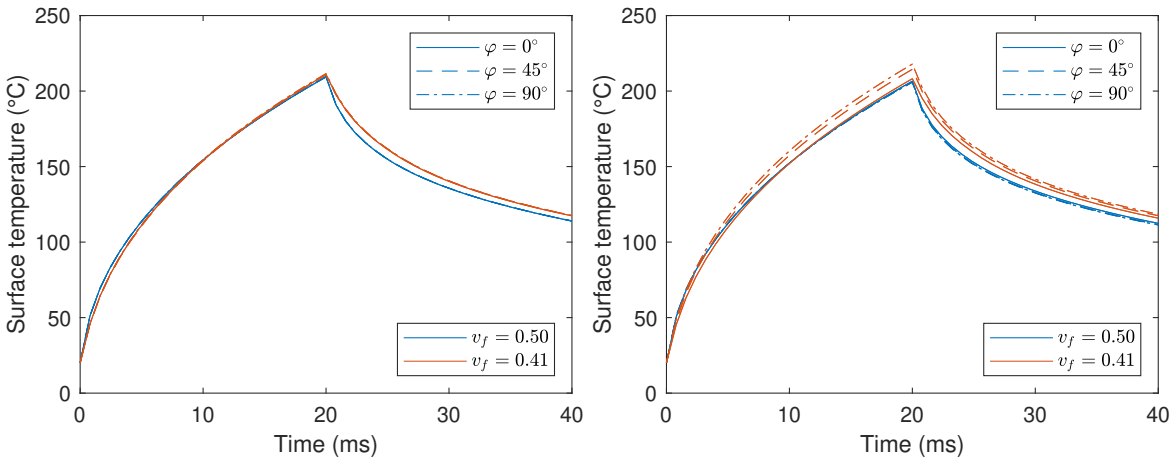


(a) $\theta = 15°$, $\phi_{laser} = 1.47\, MW.m^{-2}$.

(b) $\theta = 60°$, $\phi_{laser} = 2.793\, MW.m^{-2}$.

Fig. 17: Surface temperature evolution: effect of microstructure variability between a dense and scattered carbon fibre reinforced composite.

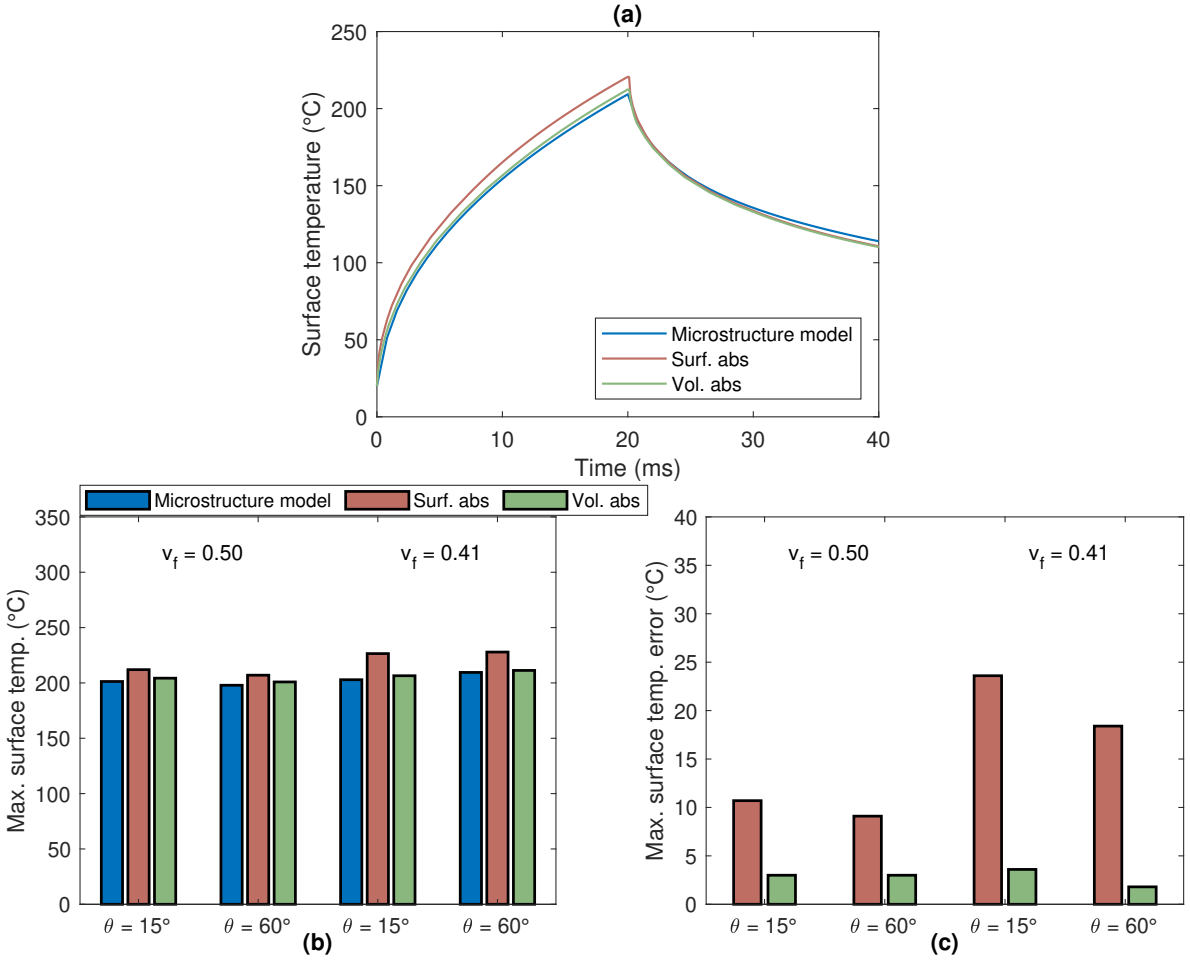


Fig. 18: (a) Surface temperature evolution of the microstructure and 1D homogenised models with surface and volumetric heat source condition in a near-normal incidence $\theta = 15°$ at $0°$ fibre orientation. (b) Maximal surface temperature and (c) end of heating surface temperature error to microstructure models. Summary of near-normal and grazing incidences on dense and scattered microstructures.

| | PEKK7002 | Carbon fibre AS7 |
|---|---|---|
| Density $\rho$ $(kg.m^{-3})$ | 1290 | 1790 |
| Thermal conductivity $k$ $(W.m^{-1}.K^{-1})$ | 0.27 | Longitudinal: 10<br>Transverse: 2.2 |
| Specific heat capacity $C_p$ $(J.kg^{-1}.K^{-1})$ | $T \leq T_g, \quad 3.35T(^\circ C) + 1017.0$<br>$T_g < T < T_f,$<br>$3.45T(^\circ C) + 1137.6$ | $-0.00295T(^\circ C)^2 +$<br>$3.493T(^\circ C) + 578.4$ |

Tab. 1: PEKK7002 and AS7 carbon fibre physical and thermal properties.

## Appendix A. Ray-tracing algorithm: computation of laser absorption

The inputs of the algorithm are the fibre orientation $\varphi$ and the laser incidence angle $\theta$. The principle of the algorithm is to discretize the laser beam with a large amount of lines regularly spaced by $\Delta d$, such as $\Delta d \lll d_f$, $d_f$ denoting the fibres diameter. Each line $\mathcal{D}_i$ initially carries the flux density $\phi_{inc,i,1}$:

$$\phi_{inc,i,1} = \phi_{laser} \tag{A.1}$$

where $\phi_{laser}$ is the laser heat flux. $\Delta x$ the line step along the $\overrightarrow{x}$ axis follows:

$$\Delta x = \frac{\Delta d}{\cos \eta} \tag{A.2}$$

The angle $\eta$ corresponds to the projection of the heat flux vector $\overrightarrow{q}$ onto the $(xy)$ plane such as:

$$\eta = \arctan\left(\frac{\tan(-\theta)}{\sin \varphi}\right) - \frac{|\sin \varphi|}{\sin \varphi}\frac{\pi}{2} \tag{A.3}$$

$$\overrightarrow{q} = \begin{pmatrix} -\sin\theta \sin\varphi & -\cos\theta & -\sin\theta\cos\varphi \end{pmatrix}^T \tag{A.4}$$

The incident ray is partially absorbed by the intersected carbon fibre and a reflected ray is created with a specular reflection model. The intersecting carbon fibre of the reflected ray is sought, and so on until the required number of reflections is reached or the reflected ray is directed towards the environment (Fig. A.19(a)). Any ray directed to one side of the microstructure is input on the other side as a periodicity condition.

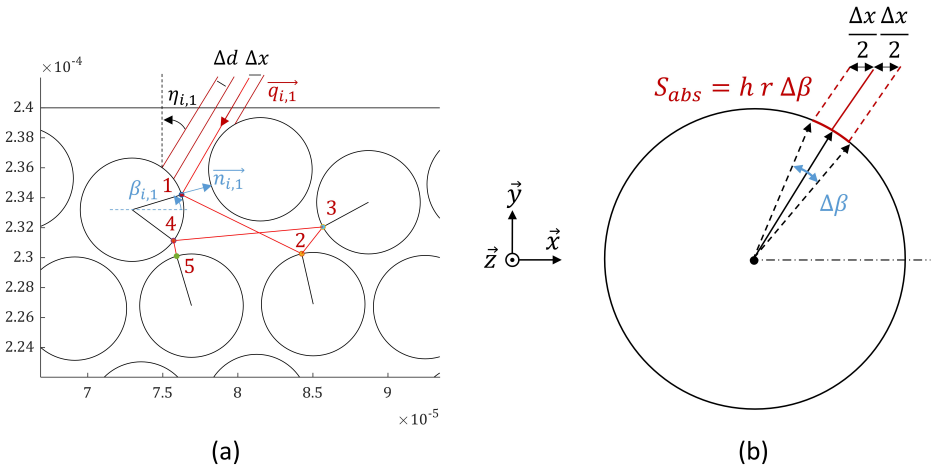


Fig. A.19: (a) Intersection of incident and reflected rays with carbon fibres, case where $\varphi = 90°$. (b) Absorption surface $S_{abs}$ determined by calculating the intersections of symmetrical rays shifted by $\pm\frac{\Delta x}{2}$.

The full algorithm is described hereinbelow:

**Algorithm 1** Ray-tracing: laser beam interaction with carbon fibres

$N_x \leftarrow \left\lfloor \dfrac{l}{\Delta x} \right\rfloor$
**for** $i = 1,\ i{+}{+},\ i \leq N_x$ **do** ▷ Incident laser rays loop
  $x_{init,1} \leftarrow i\,\Delta x$
  $y_{init,1} \leftarrow e$
  **for** $j = 1,\ j{+}{+},\ j \leq N_{refl}$ **do** ▷ Reflected rays loop
    $\overrightarrow{q_{i,j}} \leftarrow \begin{pmatrix} -\sin\theta_{i,j}\sin\varphi_{i,j} \\ -\cos\theta_{i,j} \\ -\sin\theta_{i,j}\cos\varphi_{i,j} \end{pmatrix}$
    $\eta_{i,j} \leftarrow \arctan\left(\dfrac{\tan(-\theta_{i,j})}{\sin\varphi_{i,j}}\right) - \dfrac{|\sin\varphi_{i,j}|}{\sin\varphi_{i,j}}\dfrac{\pi}{2}$
    $(x_{int}, y_{int}) \leftarrow line\_circle\_intersection(x_{init,j}, y_{init,j}, \eta_{i,j})$
    **if** $(x, y)$ exists **then** ▷ Intersection with a fibre
      $x_{i,j} \leftarrow x_{int}$
      $y_{i,j} \leftarrow y_{int}$
      $(x_1, y_1) \leftarrow line\_circle\_intersection(x_{init,j} - \dfrac{\Delta x}{2}, y_{init,j}, \eta_{i,j})$
      $(x_2, y_2) \leftarrow line\_circle\_intersection(x_{init,j} - \dfrac{\Delta x}{2}, y_{init,j}, \eta_{i,j})$
      $\Delta\beta_{i,j} \leftarrow arc\_length(x_1, y_1, x_2, y_2)$
      $\phi_{abs,i,j} \leftarrow \alpha_{carbon}\,\phi_{inc,i,j}$
      $P_{abs,i,j} \leftarrow \alpha_{abs,i,j}\,\phi_{abs,i,j}\,h\,r\,\Delta\beta_{i,j}$
      $\phi_{refl,i,j} \leftarrow \phi_{inc,i,j} - \phi_{abs,i,j}$
      $\overrightarrow{q_{r,i,j}} \leftarrow \overrightarrow{q_{i,j}} - 2(\overrightarrow{q_{i,j}} \cdot \overrightarrow{n_{i,j}})\overrightarrow{n_{i,j}}$
      $\theta_{i,j+1} \leftarrow \arccos(-q_{r,i,j,x})$
      $\phi_{i,j+1} \leftarrow \arcsin\left(\dfrac{q_{r,i,j,x}}{\sin\theta_{i,j+1}}\right)$
      $\phi_{inc,i,j} \leftarrow \phi_{refl,i,j}$
      $(x_{init,j+1}, y_{init,j+1}) \leftarrow (x_{i,j}, y_{i,j})$
    **else** ▷ The ray is reflected outside the microstructure
      $P_{abs,i,j} \leftarrow 0$
      **break**
    **end if**
  **end for**
**end for**
$\rightarrow x, y, P_{abs}$

The absorbed power $P_{abs,i}$ of $i$-th ray is computed such as:

$$P_{abs,i} = \alpha_c\,|\overrightarrow{q_i} \cdot \overrightarrow{n_i}|\,\phi_i\,S_{abs} \tag{A.5}$$

$$S_{abs,i} = h\,r\,\Delta\beta_i \tag{A.6}$$

with $S_{abs}$ the absorption surface, illustrated in Fig. A.19(b), $\phi_i$ the heat flux of $i$-th ray, $r$ the fibre radius and $h$ the extruded length.

The function $line\_circle\_intersection(x_{init}, y_{init}, \eta)$ consists in finding the first intersecting fibre of

center $(x_c, y_c)$ which intersects the ray at the point $(x, y)$. It solves following system of equations:

$$\min_{(x,y)} \left((x-x_c)^2 + (y-y_c)^2\right), \quad \begin{cases} y = y_{init} + \dfrac{x_{init} - x}{\tan\eta} \\ (y-y_c)^2 + (x-x_c)^2 = r^2 \end{cases} \tag{A.7}$$

where $(x_{init}, y_{init})$ is the ray initial point.

The function $arc\_length(x_1, y_1, x_2, y_2)$ calculates the heated fibre arc length corresponding to a ray of width $\Delta x$. Coordinates $(x_1, y_1)$ and $(x_2, y_2)$ are related to the intersecting points of symmetrical rays shifted by $\pm\dfrac{\Delta x}{2}$. The arc length $\Delta\beta$ is determined such as:

$$\Delta\beta = |\beta_1 - \beta_2| \tag{A.8}$$

$$\beta_i = \arctan\left(\frac{y_i - y_c}{x_i - x_c}\right), \quad i \in \{1, 2\} \tag{A.9}$$

The algorithm finally outputs the absorption field $\alpha$ described by the points $(x, y)$ where:

$$\alpha = \frac{P_{abs}}{P_{inc,tot}} \tag{A.10}$$

$$P_{inc,tot} = \phi_{laser}\, h\, l \tag{A.11}$$

## References


[1] P.-G. De Gennes, Reptation of a polymer chain in the presence of fixed obstacles, The journal of chemical physics 55 (2) (1971) 572–579.

[2] C. Ageorges, L. Ye, M. Hou, Advances in fusion bonding techniques for joining thermoplastic matrix composites: a review, Composites Part A: applied science and manufacturing 32 (6) (2001).

[3] A. Brasington, C. Sacco, J. Halbritter, R. Wehbe, R. Harik, Automated fiber placement: A review of history, current technologies, and future paths forward, Composites Part C: Open Access 6 (2021) 100182.

[4] K. C. Cole, I. Casella, Fourier transform infrared spectroscopic study of thermal degradation in films of poly (etheretherketone), Thermochimica acta 211 (1992) 209–228.

[5] M. Day, D. Sally, D. Wiles, Thermal degradation of poly (aryl-ether-ether-ketone): Experimental evaluation of crosslinking reactions, Journal of Applied Polymer Science 40 (9-10) (1990).

[6] P. Tadini, N. Grange, K. Chetehouna, N. Gascoin, S. Senave, I. Reynaud, Thermal degradation analysis of innovative pekk-based carbon composites for high-temperature aeronautical components, Aerospace Science and technology 65 (2017) 106–116.

[7] W. I. Lee, G. S. Springer, A model of the manufacturing process of thermoplastic matrix composites, Journal of composite materials 21 (11) (1987) 1017–1055.

[8] F. Yang, R. Pitchumani, Interlaminar contact development during thermoplastic fusion bonding, Polymer Engineering & Science 42 (2) (2002) 424–438.

[9] A. Levy, D. Heider, J. Tierney, J. W. Gillespie, Inter-layer thermal contact resistance evolution with the degree of intimate contact in the processing of thermoplastic composite laminates, Journal of Composite Materials 48 (4) (2014) 491–503.

[10] A. Khodaei, F. Shadmehri, Intimate contact development for automated fiber placement of thermoplastic composites, Composites Part C: Open Access 8 (2022) 100290.

[11] O. Çelik, D. Peeters, C. Dransfeld, J. Teuwen, Intimate contact development during laser assisted fiber placement: Microstructure and effect of process parameters, Composites Part A: Applied Science and Manufacturing 134 (2020) 105888.

[12] A. Barasinski, A. Leygue, E. Soccard, A. Poitou, Identification of non uniform thermal contact resistance in automated tape placement process, International journal of material forming 7 (4) (2014) 479–486.

[13] M. Ghasemi Nejhad, R. Cope, S. Güçeri, Thermal analysis of in-situ thermoplastic composite tape laying, Journal of Thermoplastic Composite Materials 4 (1) (1991) 20–45.

[14] F. O. Sonmez, H. T. Hahn, Modeling of heat transfer and crystallization in thermoplastic composite tape placement process, Journal of thermoplastic composite materials 10 (3) (1997) 198–240.

[15] W. Grouve, Weld strength of laser-assisted tape-placed thermoplastic composites, PhD, University of Twente, Enschede, The Netherlands (Aug. 2012).

[16] G. Dolo, Étude expérimentale et modélisation du procédé de placement de fibres avec chauffe laser, Ph.D. thesis, Université de Bretagne Sud, France (2017).

[17] C. M. Stokes-Griffin, P. Compston, A combined optical-thermal model for near-infrared laser heating of thermoplastic composites in an automated tape placement process, Composites Part A: Applied Science and Manufacturing 75 (2015) 104–115.

[18] O. Baho, G. Ausias, Y. Grohens, J. Férec, Simulation of laser heating distribution for a thermoplastic composite: Effects of afp head parameters, The International Journal of Advanced Manufacturing Technology 110 (7) (2020) 2105–2117.

[19] O. Baho, G. Ausias, Y. Grohens, M. Barile, L. Lecce, J. Férec, Automated fibre placement process for a new hybrid material: a numerical tool for predicting an efficient heating law, Composites Part A: Applied Science and Manufacturing 144 (2021) 106360.

[20] S. Grove, Thermal modelling of tape laying with continuous carbon fibre-reinforced thermoplastic, Composites 19 (5) (1988) 367–375.

[21] C. M. Stokes-Griffin, P. Compston, Optical characterisation and modelling for oblique near-infrared laser heating of carbon fibre reinforced thermoplastic composites, Optics and Lasers in Engineering 72 (2015) 1–11.

[22] B. Cosson, M. Deléglise, W. Knapp, Numerical analysis of thermoplastic composites laser welding using ray tracing method, Composites Part B: Engineering 68 (2015) 85–91.

[23] X. Ji, S. Matsuo, N. R. Sottos, D. G. Cahill, Anisotropic thermal and electrical conductivities of individual polyacrylonitrile-based carbon fibers, Carbon (2022).

[24] J. C. Maxwell, A treatise on electricity and magnetism, Vol. 1, Clarendon press, 1873.

[25] L. Rayleigh, Lvi. on the influence of obstacles arranged in rectangular order upon the properties of a medium, The London, Edinburgh, and Dublin Philosophical Magazine and Journal of Science 34 (211) (1892) 481–502.

[26] J. A. Charles, D. W. Wilson, A model of passive thermal nondestructive evaluation of composite laminates, Polymer Composites 2 (3) (1981) 105–111.

[27] M. Villière, D. Lecointe, V. Sobotka, N. Boyard, D. Delaunay, Experimental determination and modeling of thermal conductivity tensor of carbon/epoxy composite, Composites Part A: Applied Science and Manufacturing 46 (2013) 60–68.

[28] Hexcel Corporation, HexTow® AS7 Carbon Fiber (2020).

[29] Arkema Inc., Kepstan® PEKK - Polyether Ketone Ketone (2018).

[30] N. Otsu, A threshold selection method from gray-level histograms, IEEE transactions on systems, man, and cybernetics 9 (1) (1979) 62–66.

[31] P. V. Hough, Method and means for recognizing complex patterns, US Patent 3069654 (1962).

[32] I. Arganda-Carreras, V. Kaynig, C. Rueden, K. W. Eliceiri, J. Schindelin, A. Cardona, H. Sebastian Seung, Trainable weka segmentation: a machine learning tool for microscopy pixel classification, Bioinformatics 33 (15) (2017) 2424–2426.

[33] C. Geuzaine, J.-F. Remacle, Gmsh: A 3-d finite element mesh generator with built-in pre-and post-processing facilities, International journal for numerical methods in engineering 79 (11) (2009).

[34] M. Villar, C. Garnier, F. Chabert, V. Nassiet, D. Samélor, J. C. Diez, A. Sotelo, M. A. Madre, In-situ infrared thermography measurements to master transmission laser welding process parameters of pekk, Optics and Lasers in Engineering 106 (2018) 94–104.

[35] V. Le Louet, B. Rousseau, S. Le Corre, N. Boyard, X. Tardif, J. Delmas, D. Delaunay, Directional spectral reflectivity measurements of a carbon fibre reinforced composite up to 450 c, International Journal of Heat and Mass Transfer 112 (2017) 882–890.

[36] F. Hecht, New development in FreeFem++, J. Numer. Math. 20 (3-4) (2012) 251–265.

[37] A. Faghri, Y. Zhang, 6 - melting and solidification, in: Transport Phenomena in Multiphase Systems, Academic Press, Boston, 2006, pp. 421–530.

[38] V. Le Louet, S. Le Corre, N. Boyard, Y. Jarny, D. Delaunay, Capteurs de flux thermique non intrusifs pour procédés composites haute température et temps de cycle très courts, in: Congrès national de thermique SFT 2019: Thermique et industrie du futur, 2019.

[39] J. V. Beck, B. Blackwell, A. Haji-Sheikh, Comparison of some inverse heat conduction methods using experimental data, International Journal of Heat and Mass Transfer 39 (17) (1996).

[40] ISO 8302:1991(en): Thermal insulation - determination of steady-state thermal resistance and related properties — guarded hot plate apparatus (Aug. 1991).

[41] K. Mishra, B. Garnier, S. Le Corre, N. Boyard, Accurate measurement of the longitudinal thermal conductivity and volumetric heat capacity of single carbon fibers with the $3\omega$ method, Journal of Thermal Analysis and Calorimetry 139 (2) (2020) 1037–1047.

[42] O. Rodrigo, G. Bertrand, Radial thermal conductivity of a pan type carbon fiber using the 3 omega method, International Journal of Thermal Sciences 172 (2022) 107321.

[43] K. Pietrak, T. S. Wiśniewski, A review of models for effective thermal conductivity of composite materials., Journal of Power Technologies 95 (1) (2015) 14–24.

[44] M. Coulson, E. Dantras, P. Olivier, N. Gleizes, C. Lacabanne, Thermal conductivity and diffusivity of carbon-reinforced polyetherketoneketone composites, Journal of Applied Polymer Science 136 (38) (2019) 47975.